Localisation in Thin Metallic Annuli due to Diametrical Extension

Martin G. Walker* and Keith A. Seffen†

Cambridge University Engineering Department, Cambridge, United Kingdom, CB2 1PZ

The art form of kirigami has recently attracted interest from engineers and scientists for generating complex three-dimensional structures from flat sheet-like materials. When thin metal sheets are used, the deformation can become plastic and localised, allowing for permanent intricate shapes to be formed. In this study we take the illustrative case of an annular plate under diametral tension and show that its deformed shape can be considered as a spatial mechanism of localised plastic yield-lines connected to largely undeformed regions. This technique provides useful information for the design of novel permanently deployable structures.

I. Introduction

Kirigami involves the cutting and folding of thin sheets in order to generate three-dimensional shapes [1]. Unsurprisingly, kirigami has recently attracted interest from engineers and scientists working on the design, synthesis and properties of shape-changing structures. Notable applications include flexible electronics [2, 3, 4] and the fabrication of springs and other mechanical components in graphene [5, 6]. When patterns of cuts are made throughout a sheet, the cuts open up into holes when tension is applied, enabling relatively large, coordinated displacements. If, instead of cuts, holes are present, they can be made to close under globally applied compression as the material around them 'buckles' out-of-plane into a variety of three-dimensional shapes; several authors have shown this to be viable for planar micro- and nanomaterials connected to a compliant substrate [7, 8]. On the visible scale, Lamoureux et al. [9] demonstrate a kirigami-based optical tracking system for solar panels consisting of a thin elastic sheet with a set of parallel cuts. Again, the material surrounding the cuts is made to buckle out of plane, which changes the inclination of integrated panels to suit the solar zenith angle. However, tension is applied globally to foist local compression, where buckling is contingent upon the sheet being very thin. In this sense, the local deformation and orientation of the sheet is highly controllable without being attached to a substrate.

Deployable structures are a special class of shape-changing structure that are highly packaged before being unfurled into a much larger operational state. For many spacecraft applications, unfurling only needs to happen once without need of retraction. If the deployable structure in this case can remain permanently deployed, there is often no need for a supporting structure, which simplifies its design and operation as well as reducing its mass. Thin metal is an attractive material because it plasticises straightforwardly at small strains [10]. The competition between bending and stretching in thin shells under moderate displacements tends to result in smooth singly-curved surfaces, but where deformation constraints are present, we see localised bending into sharp ridges between regions of largely undeformed material—the crumpling of paper being a common example [11]. Even though the layout of ridges is random because of the unpredictable nature of crumpling, the applied effort is minimised because plastic straining is confined to the ridges. Finding a way to induce ridges controllably offers the potential to form permanent, desirable shapes with minimum effort.

Here we are inspired by the tensile buckling of kirigami structures, and the permanent creases in crumpled shells, in order to illustrate a simple deployable structure with a repeatable, permanent deformed shape. We consider a flat annular plate under diametral tension; by joining several such plates in sequence, or in rows side-by-side, a thin sheet with holes akin to a true kirigami structure can be produced. This configuration resembles expanded metal sheet (lath), however, metal lath is manufactured by a shearing process unlike

*PhD Candidate, Advanced Structures Group, Department of Engineering

†University Reader in Structural Mechanics, Department of Engineering, Member AIAA

the tensile buckling considered in this study. Describing the behaviour of such sheets is not the aim of this study. Instead, we investigate the formation of shape under tensile buckling, where plastic regions are locally formed and eventually focus into sharp ridges. Even for this simple example, we observe two possible mode shapes and ridge patterns, depending purely on the boundary conditions. We then undertake a kinematic analysis to identify an analogous spatial mechanism, which is used to obtain the geometric constraints and to estimate the extension limits.

The observation that localisation occurs during the post-buckling regime of thin-walled, cold-formed steel members led to the development of a yield-line analysis method, where the lines of localisation are assumed to form singular plastic hinges [12, 13, 14]. This approach has been used to determine the amount of plastic work required in sheet forming applications [15]. The load-deformation behaviour can be estimated by equating the work rate of the applied loads to the rate of energy dissipated by rotations of the yield-lines. This method is sometimes referred to as 'generalised' yield-line analysis in order to distinguish it from the 'classical' yield-line analysis of transversely loaded concrete slabs. A generalised yield-line analysis cannot determine the exact load-displacement behaviour [16], therefore only an approximate load-deformation curve is obtained. The quality of this approximation is dependent on how close the assumed deformation mechanism is to the true mechanism. However, unlike classical yield-line analysis, generalised yield-line analysis does not guarantee an upper-bound result since it is sometimes possible to find a kinematically admissable mechanism which predicts a lower strength than observed experimentally [14]. This precludes the optimisation of yield-line patterns done for the classical yield-line analysis of concrete slabs. We avoid this issue by using the experimentally observed mechanism and obtain a good prediction of the load-displacement behaviour.

II. Experiments and Observations

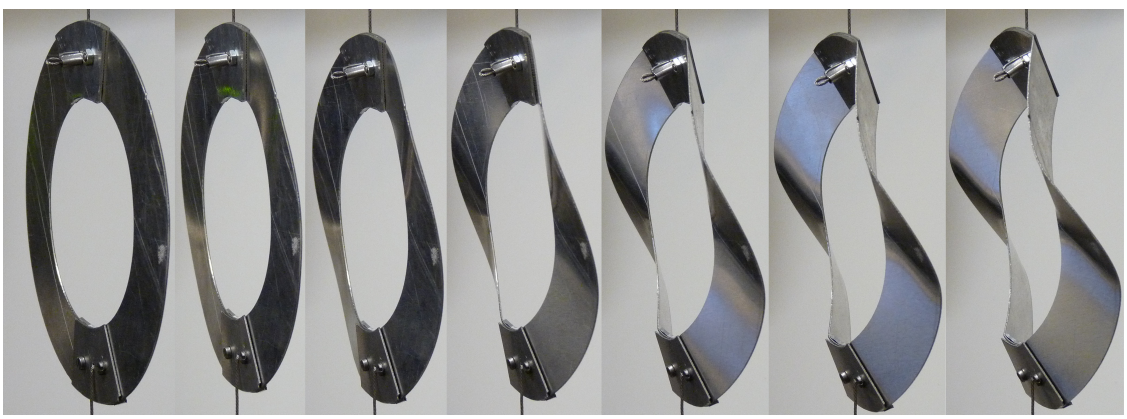

Figure 1: Deformation sequence obtained by diametrically extending an annulus while allowing the ends to rotate in the same sense. The annulus has initial internal and external diameters of 60 mm and 100 mm respectively, and a thickness of 0.5 mm.

When a thin annulus is pulled across a diameter, it quickly buckles out-of-plane and forms a smooth, oscillating transverse shape. The process is initially elastic, and plastic straining can occur later, depending on the plate thickness and deformed shape. After initial buckling, bending of the plate becomes concentrated into regions of high curvature as the rest of the annulus loses bending strain. Such localisation reaches a natural limit, after which in-plane strains dominate the deformation and the applied load increases sharply with diametral extension—leading to material yielding, and ultimately failure by tearing. The extension sequences for two annuli are shown in Figs 1 and 2, which differ only in how they are held in position; this will be discussed later. In both, their geometry is chosen so that they begin to localise plastically after tensile buckling, leaving residual out-of-plane shapes after the loading is removed, which are shown in Fig. 4.

The annuli are made from 0.5 mm thick 1050-H16 aluminium alloy with inner and outer diameters of 60 mm and 100 mm respectively. Both are loaded by pulling on 0.8 mm diameter steel cables attached at diametrical points located 10 mm from the edge (the centreline of the annulus), as shown in Fig. 3. The cables are passed through the annuli and attached to stiff support plates on the opposite face, in order to prevent the cable from 'pulling though' and to furnish control of the boundary conditions. In both, the

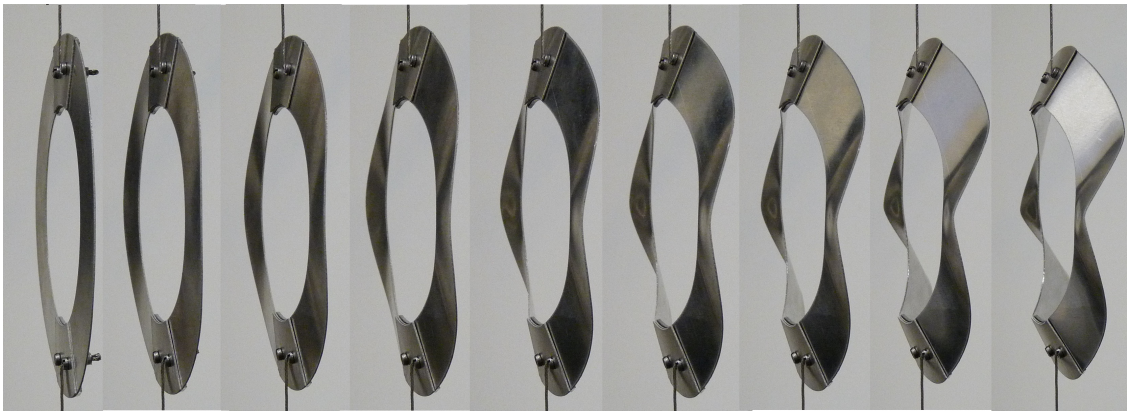

Figure 2: Diametrical extension of an annulus of the same initial geometry as Fig. 1, but allowing the ends to rotate in the opposite sense.

support plates each subtend a sector angle of 40°.

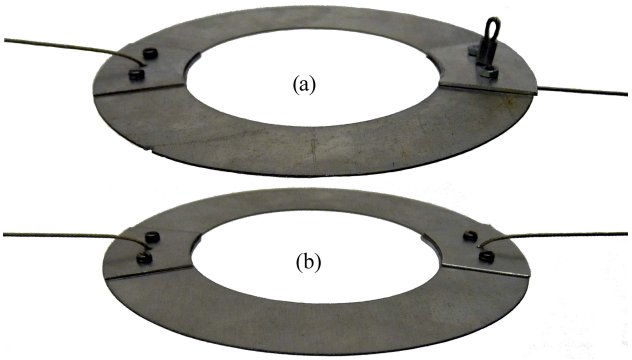

Figure 3: Cable attachment to annuli. Cables are attached to, and emerge from, opposite faces in (a) and from the same face in (b). The support plates prevent pull-through of the cable and control the boundary conditions. The sector angle of the support plates is 40°

If the cables are connected on opposite faces, see Fig. 3(a), we observe a mode shape with the support points rotated in the same sense, Fig. 4(a). Conversely, opposite-sense rotation occurs if the cables are connected on the same face, Fig. 3(b), giving a higher order mode shape, as shown in Fig. 4(b). In both cases, the support conditions must afford free rotations, otherwise in-plane stretching occurs much earlier in the loading sequence. For example, Fig. 5 shows a deformed annulus whose support rotations have been prevented; tearing occurs close to the support region because the displaced shape, which is similar to Fig. 4(a), attempts to foist compatible rotations at those points. Furthermore, if rotations are indeed prevented, it is straightforward to show that, regardless of displaced shape, the supports must move *towards* each other—contrary to the applied extension, which is impossible.

Each deformed shape in Fig. 4 exhibits clear narrow bands of localisation connected on either side by virtually undeformed regions. In Fig. 4(a), there are eight localisation bands whilst in Fig. 4(b) there are twelve. Their load-extension behaviour is reproduced in Fig. 6. During the initial linear phase, the extension is accommodated by planar ovalisation of both annuli *i.e.* by *in-plane* bending. The peak load during this phase is the tensile bucking load, and is marginally higher for Fig. 4(b) because its transverse mode shape is of higher order. In both cases, there is some reduction of the load during post-buckling, as localisation proceeds, before rising again. The unloading phases are not indicated but the final displacements ensure that both annuli are permanently shaped.

Closer investigation of the deformed shape in Fig. 4(a) reveals that the deformation is characterised by three approximately parallel planes: the two support regions and the central triangular region. It can also be seen that the localisation regions form in approximately parallel pairs, which suggests that rotations about the localisation lines—our hinge-lines—are equal in magnitude. This is easily confirmed by measuring the

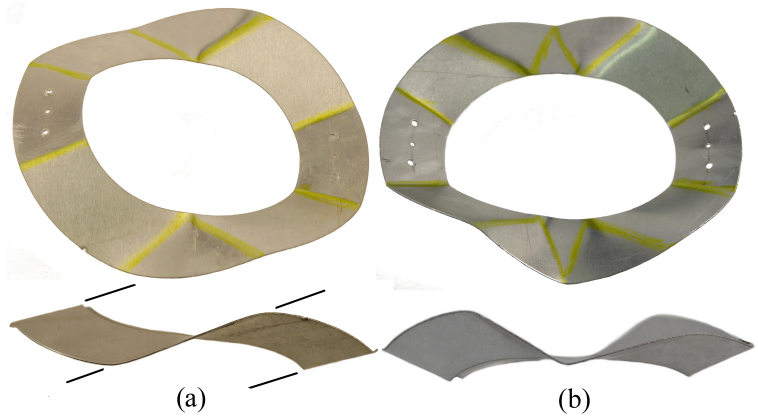

Figure 4: Residual shapes formed by diameterically extending an annulus beyond the point where plastic deformations form due to localisation, and then unloading. The annuli are made from 0.5 mm thick 1050-H16 aluminium alloy with an inner diameter of 60 mm and outer diameter of 100 mm. Both shapes are symmetrical about the extension axis. The localisation regions are highlighted as lightly coloured bands. The black lines in (a) indicate the three approximately parallel planes observed in this deformation mode.

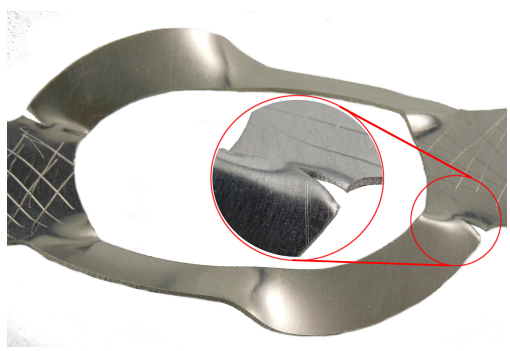

Figure 5: Deformed shape obtained while keeping diametrical supports restrained in plane. The resulting tearing can be seen in the inset.

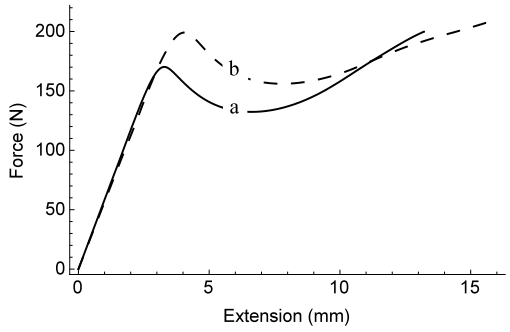

Figure 6: Load displacement curves when forming the shape in Fig. 4(a), curve (a), and Fig. 4(b), curve (b). Both curves have the same initial elastic behaviour, because the annulus geometry is identical. The buckling load and post-buckling resistance of curve (b) is higher because the mode shape is of a higher order - resulting in more yield-lines.

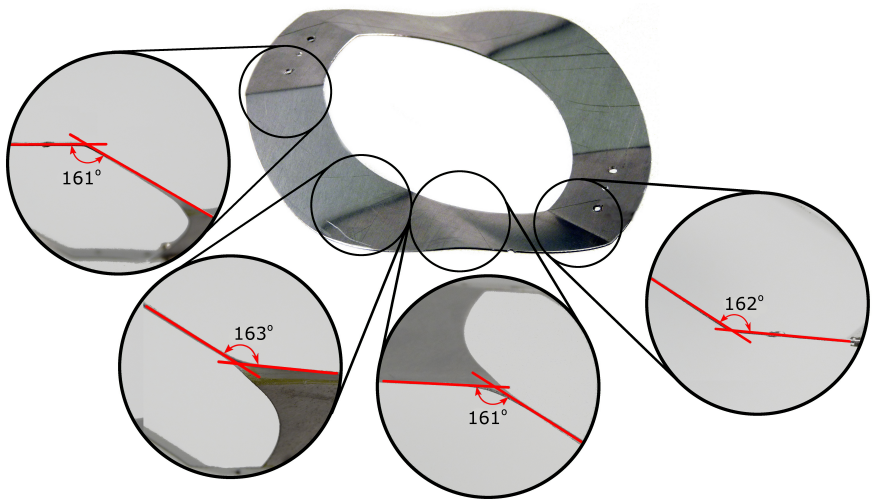

Figure 7: Measurement of hinge-line rotations of the deformed shape for an annulus with a support sector angle of 40° and inner and outer diameter of 60 mm and 100 mm respectively. Each subfigure is an axial view of the localised region, giving the relative rotations across them. As can be seen these hinge-line rotations are approximately equal.

rotation angles, as shown in Fig. 7. The angles were measured from photographs taken parallel to the hinge lines and confirmed by physical measurements with a protractor. One expectation of the following kinematic analysis is that rotation angles are predicted to be equal in magnitude.

III. Kinematic Analysis

For our analysis we omit the initial planar elastic ovalisation, which has been studied by Timoshenko and Goodier [17], because this deformation is very small in comparison. A full continuum analysis, which is complicated by the elasto-plastic interaction, is also beyond the scope of this work. In this study we recognise that the post-buckling deformation resembles a spatial mechanism with dissipative hinges: this can be investigated by employing well-established kinematic tools, in order to obtain the geometric constraints and to estimate the extension limits. When combined with generalised yield-line analysis, an approximation of the load-extension behaviour can be obtained.

Undeformed annulus regions are modelled as rigid 'links'. Thus, the annulus can only be extended by rotations of the hinge-lines and localisation begins immediately. In order to model the displaced shape as a mechanism of interconnected hinge lines, we use the transformation-matrix based approach developed by Denavit and Hartenberg [18] where each link i is connected to link $i+1$ by a hinge line, and so forth. The geometric detail of each link is not required; instead we only need to furnish the relative twist of consecutive hinge lines, α_i, the hinge angles, θ_i, and the axial separation between hinge lines, a_i, as shown in Fig. 8. The local z coordinate is always coincident with the hinge axis and orthogonal to the axes of both connected links.

The transformation matrix, T, from link $i+1$ to i can be written as [19]:

$$T_{i,i+1} = \begin{bmatrix} \cos\theta_i & -\cos\alpha_i \sin\theta_i & \sin\alpha_i \sin\theta_i & a_i \cos\theta_i \\ \sin\theta_i & \cos\alpha_i \cos\theta_i & -\sin\alpha_i \cos\theta_i & a_i \sin\theta_i \\ 0 & \sin\alpha_i & \cos\alpha_i & s_i \\ 0 & 0 & 0 & 1 \end{bmatrix} \tag{1}$$

which multiplies a position vector, R_{i+1}, in the $i+1$ coordinate system to obtain the position vector R_i, for

the same point, in the i coordinate system:

$$R_{i+1} = \begin{bmatrix} x_{i+1} \\ y_{i+1} \\ z_{i+1} \\ 1 \end{bmatrix} \tag{2}$$

The fourth row in Eqn 1 is included to make the transformation matrix square and invertible. The T matrices can be combined to transform the position vector R_{i+1} in the $i+1$ coordinate system to the coordinate system of any other link, n, according to:

$$R_n = T_{n,n+1} T_{n+1,n+2} \cdots T_{i,i+1} R_{i+1} \tag{3}$$

Equation 3 provides a set of three expressions (the fourth being '1 = 1'), expressed in terms of the hinge rotations, θ_i and the Denavit and Hartenberg parameters α_i, a_i, and s_i, which govern the kinematics of the mechanism. For a closed loop, the product of the transformation matrices around the entire chain must equal the identity matrix, providing the loop-closure constraint equations.

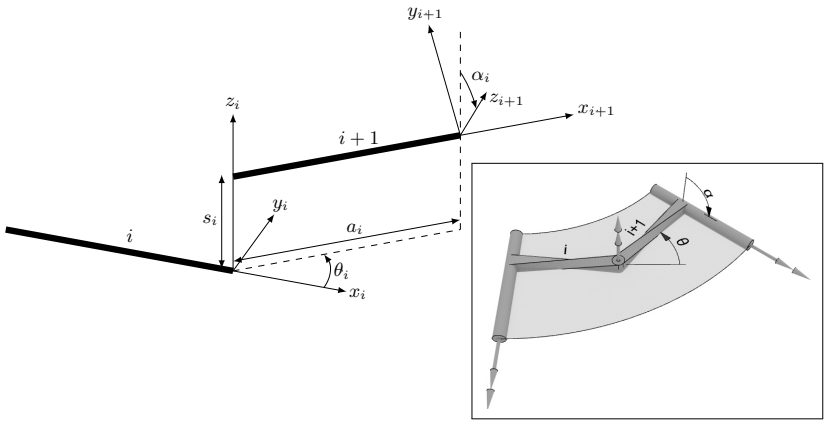

Figure 8: The Denavit-Hartenberg parameters. The parameter a_i is the distance along axis x_{i+1} from axis z_i to axis z_{i+1}. The angle α_i is the twist angle along axis x_{i+1} of axis z_{i+1} relative to axis z_i viz. the change in hinge orientation along the axis joining them. s_i is the offset along axis z_i between axis x_i and x_{i+1}, and θ_i is the rotation angle from axis x_i to axis x_{i+1} about axis z_i. The inset shows how a fixed 'dummy' hinge, oriented normal to the segment, can be used to model a curve.

We consider the annulus of Fig. 4(a) in detail only because its idealised form has fewer hinge lines, see Fig. 9, and can therefore be described more concisely. The corresponding set of Denavit-Hartenberg parameters are summarised in Table 1. We take advantage of the symmetry of the deforming annulus about the line connecting points A and B, and model only one half of it. The inner radius is b and the outer radius of the annulus is a; the sector angle Φ identifies the region between the supports which is free to deform and localise; the link lengths are l_i; and the hinge line axes are z_i, as shown in Fig. 9. The Denavit-Hartenberg model requires that all hinge lines are orthogonal to both links connecting to them. Therefore, in order to accommodate the curved geometry of the annulus, the hinges about axes z_1, z_3, z_5, z_7 and z_9 are initially oriented out of plane and rotations about these axes are fixed by the annulus geometry (see inset of Fig. 8). The hinges about axes z_2, z_4, z_6 and z_8 are naturally mobile and rotate by an angle $\theta_1, \theta_2, \theta_3, \theta_4$, respectively, according to the 'right hand rule'. The angles ϕ_2 and ϕ_3 specify the angular position with respect to axes z_3 and z_5, respectively, and are set by the annulus geometry; the angle Ψ fixes the location of axis z_3. Points A and B are located on the annulus centreline where it intersects the extension axis (where the 'dummy' hinge axes z_1 and z_9 intersect the annulus), and the distance between them, d, is used to measure the extension of the annulus.

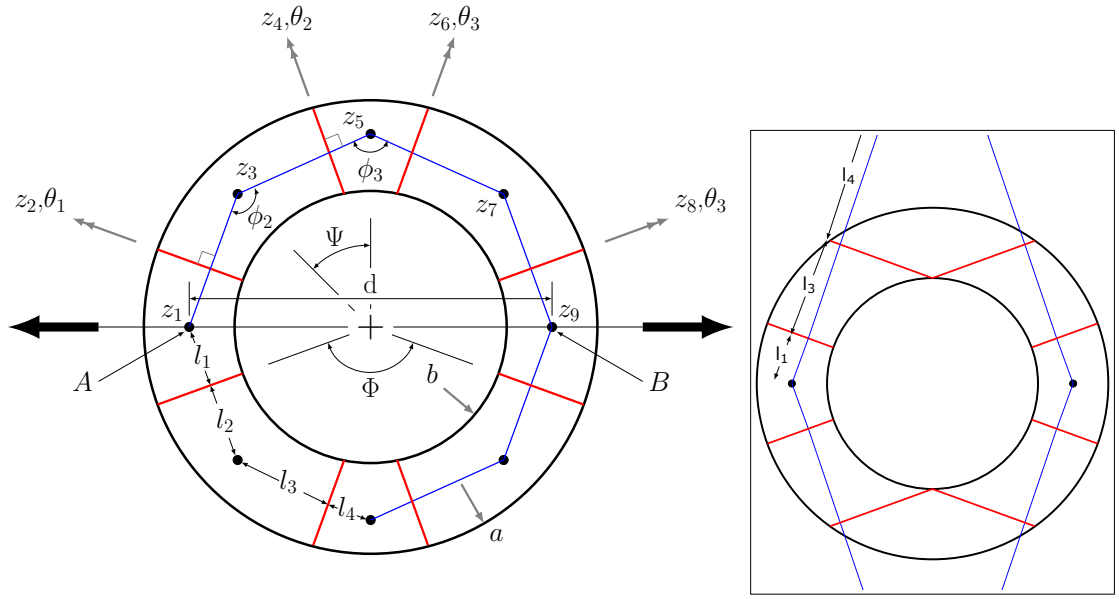

Figure 9: Initial plan view (before rotation and displacements occur) of the annulus geometry and assumed link and hinge model for the kinematic analysis. The inset shows the link and hinge model for the case of parallel hinge lines, where $l_2 = 0$ due to Eqn 4b since $\Psi = \frac{\phi}{2}$ in this case.

Table 1: Denavit-Hartenberg parameters for the annulus link and hinge model for one half of the model shown in Fig. 9. The model is symmetric about the loading axis connecting points A and B.

i	a_i	α_i	s_i	θ_i
1	l_1	$-\frac{\pi}{2}$	0	$\frac{\Phi}{2}$
2	l_2	$\frac{\pi}{2}$	0	θ_1
3	l_3	$-\frac{\pi}{2}$	0	$\phi_2 - \pi$
4	l_4	$\frac{\pi}{2}$	0	θ_2
5	l_4	$-\frac{\pi}{2}$	0	$\phi_3 - \pi$
6	l_3	$\frac{\pi}{2}$	0	θ_3
7	l_2	$-\frac{\pi}{2}$	0	$\phi_2 - \pi$
8	l_1	$\frac{\pi}{2}$	0	θ_4

The link lengths l_1, l_2, l_3 and the angle ϕ_2 can be computed from the ring radii, a and b, the sector angle Φ, and the parameters Ψ, ϕ_3, and l_4, as:

$$l_1 = \frac{a+b}{2}\cos\left(\frac{\Phi}{2}\right) \tag{4a}$$

$$l_2 = \frac{a+b}{2}\sin\left(\frac{\Phi}{2}\right)\tan\left(\frac{\Phi}{2} - \Psi\right) \tag{4b}$$

$$l_3 = \frac{(a+b)\sin\left(\frac{\Phi}{2}\right)\sin(\Psi)}{2\sin\left(\frac{\phi_3}{2}\right)\cos\left(\frac{\Phi}{2} - \Psi\right)} - l_4 \tag{4c}$$

$$\phi_2 = \frac{3\pi - \Phi - \phi_3}{2} \tag{4d}$$

which can be simplified by observing that, in experiments, yield-lines occur in approximately parallel pairs, whence:

$$\phi_3 = \pi - \Phi \qquad \phi_2 = \pi \qquad \Psi = \frac{\Phi}{2}$$

This forces $l_2 = 0$ according to Eqn 4b. The link length l_4 fixes where hinge lines z_4 and z_6 intersect. While this length can be selected arbitrarily, the hinge lines z_4 and z_6 are observed to intersect at the inner edge of the annulus in the final deformed shape, as shown in Fig. 4. Therefore:

$$l_4 = \frac{\sin\left(\frac{\Phi}{2}\right)}{2}\left((a+b)\tan\left(\frac{\Phi}{2}\right) - 2b\right) \tag{5}$$

and

$$l_3 = b\sin\left(\frac{\Phi}{2}\right) \tag{6}$$

The layout of the resulting link and hinge model is shown in the inset of Fig. 9. Using the parameters in Table 1, Eqn 3 can be used to express the coordinates of point B relative to point A, resulting in three, nonlinear and highly coupled equations in terms of the angles θ_i and the annulus geometry. We have not assumed any relationship between these angles *a priori*; since these equations cannot be solved analytically, we apply a constrained optimisation procedure using Matlab [20] to obtain the relationship between the angles θ_i numerically for a variety of annulus extensions and geometries. In each case the magnitude of the hinge rotations was equal, and thus we can infer with reasonable certainty that the relationship between the hinge rotations, θ_i is:

$$\theta_1 = -\theta_2 = \theta_3 = -\theta_4 = \pm\theta \tag{7}$$

which is confirmed by the experimental observation of equal rotation magnitudes. The corresponding dimensionless straight-line distance between points A and B, d/d_0, can therefore be simplified to (see derivations in Appendix A):

$$\frac{d}{d_0} = \frac{1}{\rho+1}\sqrt{4\rho^2\sin^2\theta\sin^2(\Phi/2) + [\rho + \rho(\cos\theta - 1)\sin\Phi + 1]^2} \tag{8}$$

where $b/a = \rho$ and $d_0 = d|_{\theta=0} = a + b$.

By maximising Eqn 8 with respect to θ we obtain the hinge rotation, θ_{max}, which gives the maximum elongation, d_{max} as:

$$\theta_{max} = \cos^{-1}\left(\frac{\sin\Phi(1 - \rho\sin\Phi + \rho)}{4\rho\sin^4(\Phi/2)}\right) \tag{9}$$

and then, after substituting into Eqn 8:

$$\frac{d_{max}}{d_0} = \sqrt{\frac{4\rho^2(\sin\Phi + \cos\Phi) + 4\rho\sin\Phi - 2\rho(3\rho+2) + 2}{(\rho+1)^2(\cos\Phi - 1)}} \tag{10}$$

The influence of ρ in this expression is shown in Fig. 10(a). The largest elongation increases as ρ approaches unity. For positive elongation ($d/d_0 > 1$), $d|_{\theta=0}$ must be a minimum, which enforces a lower limit upon ρ:

$$\rho > \frac{1}{2\tan(\Phi/2) - 1} \tag{11}$$

Equation 10 also depends on Φ, and Fig. 10(b) indicates the variation for a nominal value of $\rho = 0.7$. Larger elongations occur when the sector angle approaches 180° but there is also a lower limit on Φ that ensures $d/d_0 > 1$:

$$\Phi > \cos^{-1}\frac{(\rho-1)(3\rho+1)}{\rho(5\rho+2)+1} \tag{12}$$

These constraints can be used to establish if a particular localisation mechanism can be achieved and allow an appropriate geometry to be selected. The sector angle, Φ, will typically be fixed by the application boundary conditions, in which case Eqn 11 can be used to determine the minimum ratio of inner to outer radii, ρ, for extension of the mechanism, and thus localisation, to be possible. Additionally, Eqn 10 provides the maximum mechanism extension possible beyond which stretching and tearing must occur.

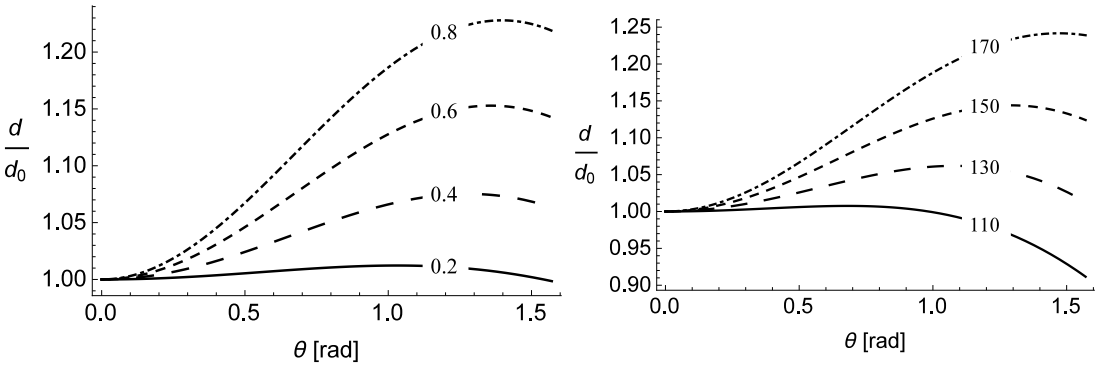

(a) Influence of ρ for $\Phi = 160°$

(b) Influence of Φ for $\rho = 0.7$

Figure 10: Normalised elongation (d/d_0) variation with hinge rotation (θ). Plots are symmetrical about the $\theta = 0$ axis. Larger ρ ratios have a greater elongation capacity. Similarly, the elongation capacity increases as the sector angle, Φ, increases.

IV. Generalised yield-line analysis

A generalised yield-line analysis now reveals the relationship between the applied extension load and the hinge rotations using the kinematic model developed in the previous section. We assume that hinge lines behave as singular yield-lines of plastic moment resistance per unit length, m_p. We also neglect in-plane normal and shear stresses which have the effect of reducing m_p [21]. The relationship between the applied elongation load and the hinge rotations can then be solved by equating the rate of energy dissipated by rotations of the yield-lines to the work rate of the applied load: the latter term is equal to the applied elongation force, F, multiplied by the extension-rate along the line of action connecting A and B, $\dot{d}$, where ($\dot{}$) represents the time derivative [16]:

$$\dot{W} = F\dot{d} = F\frac{\mathrm{d}d}{\mathrm{d}\theta}\dot{\theta} = \sum_{i=1}^{n} m_p \dot{\theta}_i l_i \tag{13}$$

where $\dot{W}$ is the work rate, n is the number of yield lines, $\dot{\theta}_i$ is the rotation rate of hinge line i, and l_i is the length of yield-line i. Since d depends only on θ and geometrical constants (see Eqn 8) and $|\dot{\theta}_i| = \dot{\theta}$ according to Eqn 7, the $\dot{\theta}$ terms in Eqn 13 cancel providing an expression relating the applied elongation force, F, to the hinge rotations, θ:

$$\frac{F}{m_p} = \frac{L^* \sqrt{4\rho^2 \sin^2\theta \sin^2(\Phi/2) + (\rho + \rho(\cos\theta - 1)\sin\Phi + 1)^2}}{2\rho \sin\theta \sin(\Phi/2)\left(2\rho\cos\theta\sin^3(\Phi/2) + \cos(\Phi/2)(\rho\sin\Phi - \rho - 1)\right)} \tag{14}$$

where,

$$L^* = 2\sqrt{2\rho^2\cos^2\Phi - 2\rho^2 + 4} - 8\rho\cos^2\left(\frac{\Phi}{4}\right) + 4$$

which is the total length of yield lines divided by the outer radius a. Note from Eqn 14 that F does not depend on the absolute size of the annulus, only on the ratio ρ, the sector angle Φ, and the plastic moment resistance per unit length m_p. In order to obtain the load-extension behaviour shown in Fig. 11, the hinge rotations, θ, in Eqn 14 are related to the extension, d/d_0, using Eqn 8. In the extreme, the load tends to infinity at displacement limits of $d = d_0$ and $d = d_{max}$. In practice, in-plane stretching dominates beyond these limits, but recall that we do not allow stretching in this model. Between these limits the load quickly drops and remains approximately constant for a range of d. Similar behaviour has been observed for other tension-activated kirigami structures [22].

V. Comparison to experiments

The kinematic and generalised yield-line analyses are now compared to experiments. The plastic moment capacity per unit length, m_p, is needed to compute the magnitude of the load-elongation behaviour. The

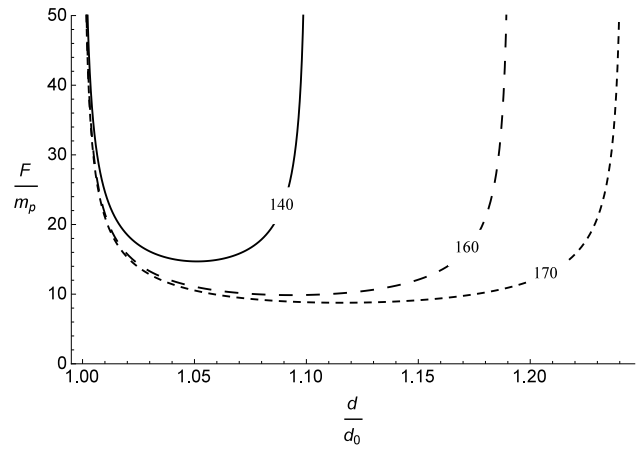

Figure 11: Nondimensionalised load-displacement behaviour of the link-hinge model for sector angles (Φ) of 140°, 160°, and 170° with $\rho = 0.7$.

yield stress, σ_y, of 1050-H16 aluminium alloy is 124 MPa [23], which results in a plastic moment capacity per unit length $m_p = t^2\sigma_y/4 = 7.75$ N for a 0.5 mm thick sheet. This was confirmed with three-point bending tests, Fig. 12, where m_p is indicated.

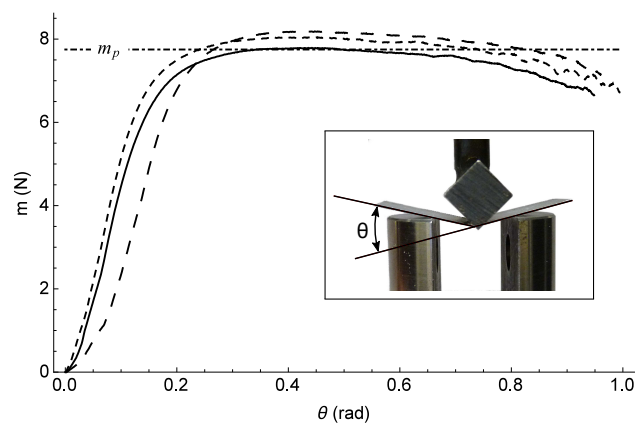

Figure 12: Load-rotation results from the 3-point bending tests. The assumed value of m_p is indicated, as is the bending moment per unit length, m, in the centre of the strip under the loading point. The relative rotation angle, θ, and the loading configuration are shown in the inset.

The load-displacement behaviour predicted by the present model is compared to experiments in Figs 13 to 16, where zero extension is taken as the extension at buckling—the beginning of localisation if we neglect in-plane elastic deformation. The generalised yield-line model over-predicts the load measured in the tests. This is due to two main factors: the approximate prediction of the post-buckling load displacement behaviour provided by the generalised yield-line approach, and the effect of axial load on the plastic moment capacity of the yield-lines. The presense of axial load on a yield-line has the effect of reducing the plastic moment capacity. This has been studied by various authors including Hiriyur and Schafer [14] and Bakker [16], however, there is little agreement on how to correctly incorporate this effect [14]. We show an example of the effect of axial load by using a simple model proposed by Hiriyur and Schafer [14] in Appendix B, where the predicted load is reduced to approximately the same range and below the measured values.

The prediction of the maximum displacement of the assumed mechanism is also indicated. In tests, there is no clear point where localisation stops and stretching begins to dominate, however, it is clear from Figs 13 to 15 that the predicted maximum extension is smaller than the extension at failure, and falls in the region where tests show the load increasing towards failure after reaching a minimum value. Thus, the kinematic model provides a useful method for understanding the deformation limits for the localisation process as well as the influence of the sector angle and ratio of inner to outer radii on the extension behaviour. In turn, the

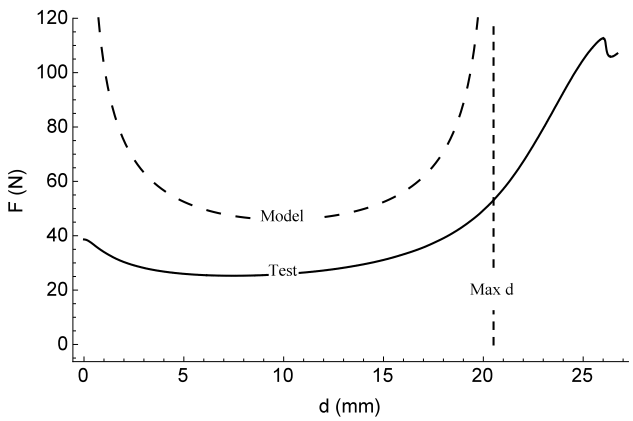

Figure 13: Comparison of experiment to model for a sector angle of $\Phi = 160°$ and $\rho = 0.8$.

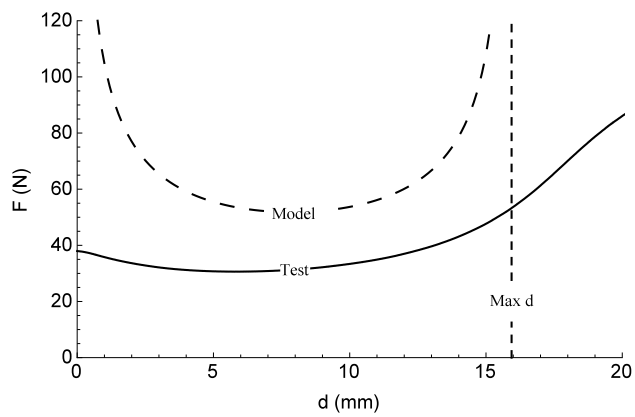

Figure 14: Comparison of experiment to model for a sector angle of $\Phi = 150°$ and $\rho = 0.8$.

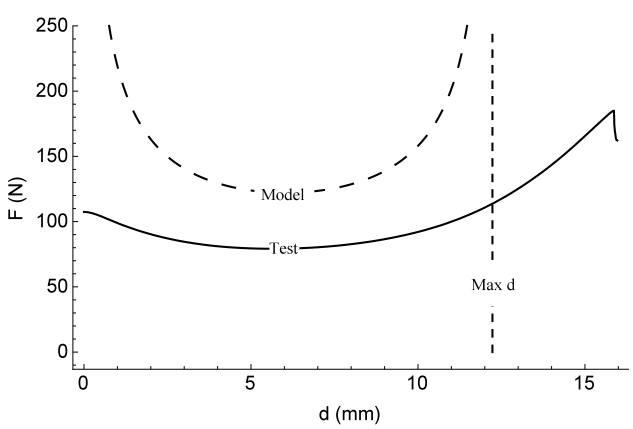

Figure 15: Comparison of experiment to model for a sector angle of $\Phi = 160°$ and $\rho = 0.6$.

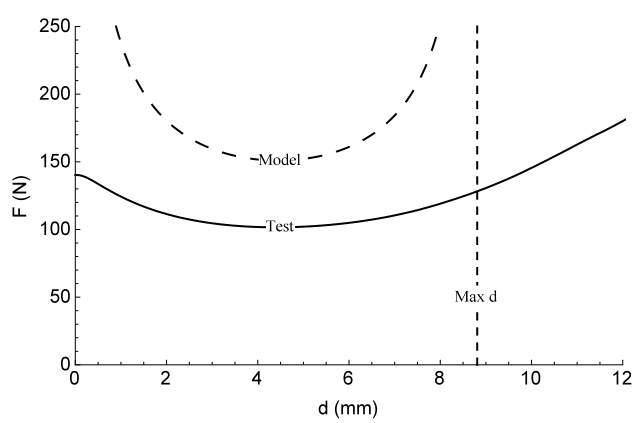

Figure 16: Comparison of experiment to model for a sector angle of $\Phi = 150°$ and $\rho = 0.6$.

kinematics inform the generalised yield-line model, which then provides an estimate of the load-deformation behaviour of the annular plate.

VI. Discussion

We have considered the localisation of deformation in annular plates subjected to diametrical extension. Two different, symmetrical, localisation patterns were obtained by varying the support conditions at the extension points. If the ends are permitted to rotate in equal senses, a pattern consisting of eight localisation lines connected by eight predominately undeformed regions is observed; if the ends are permitted to rotate in opposite senses, a pattern consisting of twelve localisation lines connected by twelve predominately undeformed regions is obtained; if the ends are restrained in plane, localisation does occur, but this accompanied by tearing.

In order for deformations to localise without tearing or in-plane stretching, a spatial mechanism must exist, which consists of the localisation regions as hinges and the regions between them as rigid links. As an illustrative example, the kinematics of the spatial mechanism corresponding to the equal sense case was analysed and used to establish the geometric, and deformation limits under diametrical extension. Using generalised yield-line analysis, an estimate of the load-displacement behaviour was also obtained.

Our processes yield useful information about the geometric limits, deformation behaviour, and the load-deformation relationship. We assert that they may be applied more generally to kirigami sheets where fold lines have not been prescribed but form through the localisation of deformations. This allows a kirigami sheet to be permanently formed into a new shape through the application of simple deformations. Taking advantage of plastic localisation as a shape-forming mechanism has applications for deployable structures that permanently remain in the deployed configuration.

References

[1] Robin M. Neville, Fabrizio Scarpa, and Alberto Pirrera. Shape morphing Kirigami mechanical metamaterials. *Scientific Reports*, 6:31067, 2016. ISSN 2045-2322. doi: 10.1038/srep31067.

[2] Changsheng Wu, Xin Wang, Long Lin, Hengyu Guo, and Zhong Lin Wang. Paper-based triboelectric nanogenerators made of stretchable interlocking kirigami patterns. *ACS Nano*, 10(4):4652–4659, 2016. ISSN 1936-0851. doi: 10.1021/acsnano.6b00949.

[3] Zeming Song, Xu Wang, Cheng Lv, Yonghao An, Mengbing Liang, Teng Ma, David He, Ying-Jie Zheng, Shi-Qing Huang, Hongyu Yu, and Hanqing Jiang. Kirigami-based stretchable lithium-ion batteries. *Scientific Reports*, 5:10988, 2015. ISSN 2045-2322. doi: 10.1038/srep10988.

[4] Terry C. Shyu, Pablo F. Damasceno, Paul M. Dodd, Aaron Lamoureux, Lizhi Xu, Matthew Shlian, Max Shtein, Sharon C. Glotzer, and Nicholas a. Kotov. A kirigami approach to engineering elasticity in nanocomposites through patterned defects. *Nature Materials*, 14:785–789, 2015. ISSN 1476-1122. doi: 10.1038/nmat4327.

[5] Melina K. Blees, Arthur W. Barnard, Peter a. Rose, Samantha P. Roberts, Kathryn L. McGill, Pinshane Y. Huang, Alexander R. Ruyack, Joshua W. Kevek, Bryce Kobrin, David a. Muller, and Paul L. McEuen. Graphene kirigami. *Nature*, 524:204–207, 2015. ISSN 0028-0836. doi: 10.1038/nature14588.

[6] Zenan Qi, David K. Campbell, and Harold S. Park. Atomistic simulations of tension-induced large deformation and stretchability in graphene kirigami. *Physical Review B - Condensed Matter and Materials Physics*, 90(24):245437, 2014. ISSN 1550235X. doi: 10.1103/PhysRevB.90.245437.

[7] Sheng Xu, Zheng Yan, Kyung-In Jang, Wen Huang, Haoran Fu, Jeonghyun Kim, Zijun Wei, Matthew Flavin, Joselle McCracken, Renhan Wang, Adina Badea, Yuhao Liu, Dongqing Xiao, Guoyan Zhou, Jungwoo Lee, Ha Uk Chung, Huanyu Cheng, Wen Ren, Anthony Banks, Xiuling Li, Ungyu Paik, Ralph G. Nuzzo, Yonggang Huang, Yihui Zhang, and John A. Rogers. Assembly of micro/nanomaterials into complex, three-dimensional architectures by compressive buckling. *Science*, 347(6218):154–159, 2015. ISSN 0036-8075. doi: 10.1126/science.1260960.

[8] Yihui Zhang, Zheng Yan, Kewang Nan, Dongqing Xiao, Yuhao Liu, Haiwen Luan, Haoran Fu, Xizhu Wang, Qinglin Yang, Jiechen Wang, Wen Ren, Hongzhi Si, Fei Liu, Lihen Yang, Hejun Li, Juntong Wang, Xuelin Guo, Hongying Luo, Liang Wang, Yonggang Huang, and John A Rogers. A mechanically driven form of kirigami as a route to 3D mesostructures in micro/nanomembranes. *Proceedings of the National Academy of Sciences*, 112(38):11757–11764, 2015. ISSN 1091-6490. doi: 10.1073/pnas.1515602112.

[9] Aaron Lamoureux, Kyusang Lee, Matthew Shlian, Stephen R Forrest, and Max Shtein. Dynamic kirigami structures for integrated solar tracking. *Nature Communications*, 6:8092, 2015. ISSN 2041-1723. doi: 10.1038/ncomms9092.

[10] Mark Schenk, Andrew D. Viquerat, Keith a. Seffen, and Simon D. Guest. Review of inflatable booms for deployable space structures: packing and rigidization. *Journal of Spacecraft and Rockets*, 51(3): 762–778, 2014. ISSN 0022-4650. doi: 10.2514/1.A32598.

[11] M. Ben Amar and Y. Pomeau. Crumpled paper. *Proceedings of the Royal Society A: Mathematical, Physical and Engineering Sciences*, 453:729–755, 1997. ISSN 1364-5021. doi: 10.1098/rspa.1997.0041.

[12] V. Ungureanu, M. Kotełko, R.J. Mania, and D. Dubina. Plastic mechanisms database for thin-walled cold-formed steel members in compression and bending. *Thin-Walled Structures*, 48:818–826, 2010. ISSN 02638231. doi: 10.1016/j.tws.2010.01.004.

[13] X.-L. Zhao. Yield line mechanism analysis of steel members and connections. *Progress in Structural Engineering and Materials*, 5(4):252–262, 2003. ISSN 1365-0556. doi: 10.1002/pse.161.

[14] B. K. J. Hiriyur and B. W. Schafer. Yield-line analysis of cold-formed steel members. *International Journal of Steel Structures*, 5(1):43–54, 2005.

[15] W. Johnson and T.X. Yu. Angle of Fold and the Plastic Work Done in the Folding of Developable Flat Sheets of Metal. *Journal of Mechanical Engineering Science*, 22(5):233–241, 1980. ISSN 00222542.

[16] M. C. M. Bakker. Yield line analysis of post-collapse behavior of thin-walled steel members. *Heron*, 35 (3), 1990.

[17] S.P. Timoshenko and J. N. Goodier. *Theory of Elasticity*. McGraw-Hill, London, 3rd edition, 1970.

[18] J. Denavit and R.S. Hartenberg. A kinematic notation for lower-pair mechanisms based on metrics. *Journal of Applied Mechanics*, 22(2):215–221, 1955.

[19] J.E. Shigley and J.J Uicker. *Theory of Machines and Mechanisms*. McGraw-Hill, 2nd edition, 1995.

[20] The Mathworks Inc. Matlab R2014b, 2014.

[21] J.M.M. Out. Yield Surface for bending moment, shear force and normal force. *Heron*, 30(4):30–58, 1985.

[22] Midori Isobe and Ko Okumura. Initial rigid response and softening transition of highly stretchable kirigami sheet materials. *Scientific Reports*, 6:24758, 2016. ISSN 2045-2322. doi: 10.1038/srep24758.

[23] LLC. MatWeb. Aluminum 1050-H16, 2016. URL `www.matweb.com`.

A. Derivations

From Fig. 17 we can see that:

$$l_1 = \frac{a+b}{2}\sin\left(\frac{\pi-\Phi}{2}\right) = \frac{a+b}{2}\cos\left(\frac{\Phi}{2}\right) \tag{15}$$

$$l_2 = \frac{a+b}{2}\sin\left(\frac{\Phi}{2}\right)\tan\left(\frac{\Phi}{2}-\Psi\right) \tag{16}$$

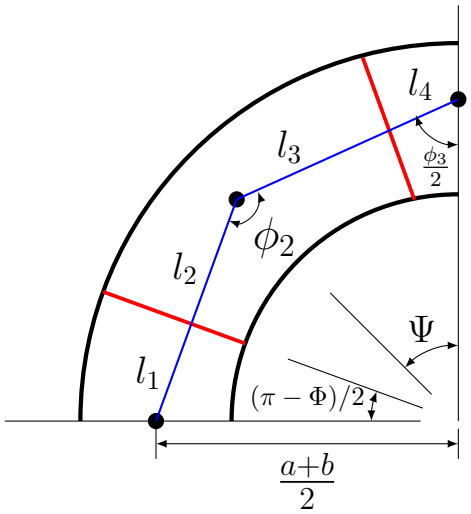

Figure 17: Quarter of D-H model

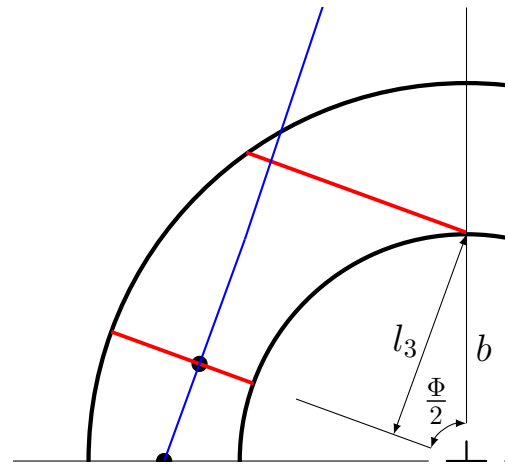

Figure 18: Calculation of l_3

Using sine law we calculate l_3:

$$\frac{\sin\Psi}{l_3+l_4} = \frac{\sin\left(\frac{\phi_3}{2}\right)\cos\left(\frac{\Phi}{2}-\Psi\right)}{\left(\frac{a+b}{2}\right)\sin\left(\frac{\Phi}{2}\right)} \implies l_3 = \frac{(a+b)\sin\left(\frac{\Phi}{2}\right)\sin(\Psi)}{2\sin\left(\frac{\phi_3}{2}\right)\cos\left(\frac{\Phi}{2}-\Psi\right)} - l_4 \tag{17}$$

In order to calculate ϕ_2 the sum of angles in the quadrant is:

$$\left(\pi - \frac{\pi}{2} - \frac{\pi-\Phi}{2}\right) + \phi_2 + \frac{\phi_3}{2} + \frac{\pi}{2} = 2\pi \implies \phi_2 = \frac{3\pi - \Phi - \phi_3}{2}$$

Assuming the hinge lines occur in approximately parallel pairs we can set:

$$\phi_3 = \pi - \Phi \qquad \phi_2 = \pi \qquad \Psi = \frac{\Phi}{2}$$

from which we get:

$$l_2 = 0 \qquad l_3 = \frac{(a+b)\sin^2\left(\frac{\Phi}{2}\right)}{2\cos\left(\frac{\Phi}{2}\right)} - l_4 \tag{18a}$$

The final parameter, l_4, fixes where hinge lines z_4, and z_6 intersect. The configuration which permits the largest elongation occurs when the hinge lines intersect at the inner edge of the annulus. From Fig 18, we can calculate l_3 to be:

$$l_3 = b\sin\left(\frac{\Phi}{2}\right) \tag{19}$$

Then using Eqn 18:

$$l_4 = \frac{(a+b)\sin^2\left(\frac{\Phi}{2}\right)}{2\cos\left(\frac{\Phi}{2}\right)} - b\sin\left(\frac{\Phi}{2}\right) \tag{20}$$

If we assume that all hinge line rotation angles have the same magnitude, θ, and remain in these proportions throughout the extension behaviour the distance between points A and B can be simplified to:

$$x = 2\cos\left(\frac{\Phi}{2}\right)(l_1 + l_3\cos(\theta) + l_4) \qquad y = 2l_3\sin\theta \tag{21a}$$

$$d = \sqrt{x^2+y^2} \tag{21b}$$

Equation 21b can be non-dimensionalised by the initial diameter $d_0 = a + b$ and taking $\frac{b}{a} = \rho$:

$$\hat{d} = \frac{d}{d_0} = \frac{\sqrt{4\rho^2 \sin^2(\theta) \sin^2\left(\frac{\Phi}{2}\right) + (\rho(\cos(\theta) - 1)\sin(\Phi) + \rho + 1)^2}}{\rho + 1} \tag{22}$$

Using Eqn 22 we can compute the load rotation behaviour using the principal of virtual velocities:

$$m_p \sum_{i=1}^{n} \dot{\theta} z_i = \dot{F} \tag{23a}$$

$$4m_p \left(|z_2| + |z_4|\right) \dot{\theta} = F \left(\frac{dx}{d\theta} \dot{\theta} \cos\left(\theta_f\right) + \frac{dy}{d\theta} \dot{\theta}_i \sin\left(\theta_f\right) \right) \tag{23b}$$

where, the lengths of the hinge lines are:

$$|z_2| = a - b \tag{24a}$$

$$|z_4| = \sqrt{b^2 \cos^2\left(\frac{\Phi}{2}\right) + a^2 - b^2} - b \cos\frac{\Phi}{2} \tag{24b}$$

m_p is the plastic hinge capacity per unit length, and θ_f is load inclination angle:

$$\tan\theta_f = \frac{x}{y} \qquad \sin\theta_f = \frac{x}{d} \qquad \cos\theta_f = \frac{y}{d} \tag{25}$$

Therefore, substituting into Eqn 23 and rearranging:

$$F = \frac{4m_p \left(|z_2| + |z_4|\right) \sqrt{4b^2 \sin^2\theta \sin^2\left(\Phi/2\right) + \left(a + b(\cos\theta - 1)\sin\Phi + b\right)^2}}{2b \sin\theta \sin\left(\frac{\Phi}{2}\right) \left[2b \cos\theta \sin^3\left(\frac{\Phi}{2}\right) - \cos\left(\frac{\Phi}{2}\right)\left(a - b\sin\Phi + b\right)\right]} \tag{26}$$

Which can be non-dimensionalised by dividing both sides by m_p and then dividing the top and bottom of the right side by a^2:

$$\frac{F}{m_p} = \frac{L^* \sqrt{4\rho^2 \sin^2\theta \sin^2\left(\Phi/2\right) + \left(\rho + \rho(\cos\theta - 1)\sin\Phi + 1\right)^2}}{2\rho \sin\theta \sin\left(\Phi/2\right)\left(2\rho \cos\theta \sin^3\left(\Phi/2\right) + \cos\left(\Phi/2\right)\left(\rho \sin\Phi - \rho - 1\right)\right)} \tag{27}$$

where we have taken:

$$L^* = 4\frac{|z_2| + |z_4|}{a} = 2\sqrt{2\rho^2 \cos^2\Phi - 2\rho^2 + 4} - 8\rho \cos^2\left(\frac{\Phi}{4}\right) + 4 \tag{28}$$

B. Plastic moment capacity of an inclined yield line under axial load

In this paper we have not considered the effect of axial load on the plastic moment capacity of a hinge line. This has been studied by various authors including Hiriyur and Schafer [14] and Bakker [16]. Axial load has the effect of reducing the plastic moment capacity. The most common approach taken to incorporate this effect involves assuming a central core carries the axial load while the remaining thickness provides the bending resistance. There is considerable disagreement on how to correctly incorporate the effect of axial load. Hiriyur and Schafer [14] provide a review of seven different models which show a very wide variation in predictions. This issue is beyond the scope of this paper, however, the possible effect of axial load is considered using the simple model for the plastic moment capacity of a yield line inclined to an axial load provided by Hiriyur and Schafer [14]:

$$M_{ph} = \frac{\lambda L \sigma_y t^2}{4} \left(1 - \left(\frac{F}{\lambda \sigma_y t L}\right)^2\right) \tag{29}$$

where,

$$\lambda = \frac{\sqrt{3}}{2} + \frac{\cos 2\beta}{2\sqrt{3}} \tag{30}$$

L is the length of the yield line, σ_y is the material yield stress, F is the applied axial load, t is the plate thickness, and β is the inclination of the yield line to the load ($\beta = 0$ indicates the yield line is perpendicular to the load). In the case of the annuli considered in the present study, $\beta = \Phi/2$. Incorporating this into Eqn 13 results in:

$$F = \frac{4\lambda\, b\, a\, L^* \sigma_y \sin\theta \sin\frac{\phi}{2}\left(2b\cos\theta\sin^3\frac{\phi}{2} - \cos\frac{\phi}{2}\left(a - b\sin\phi + b\right)\right)}{\sqrt{\left[a + b(\cos\theta - 1)\sin\phi + b\right]^2 + 4b^2\sin^2\theta\sin^2\frac{\phi}{2}}} \left(-1 + \sqrt{\frac{t^2\csc^2\theta\left(\left[a + b(\cos\theta - 1)\sin\phi + b\right]^2 + 4b^2\sin^2\theta\sin^2\frac{\phi}{2}\right)}{16b^2\sin^2\frac{\phi}{2}\left(\cos\frac{\phi}{2}(a - b\sin\phi + b) - 2b\cos\theta\sin^3\frac{\phi}{2}\right)^2} + 1} \right) \tag{31}$$

This now includes a dependence on the annulus thickness, t. The load-displacement predictions using Eqn 31 are compared to experiments and Eqn 14, which does not consider the effect of axial load on inclined yield lines, in Figs 19 to 22. The model which includes the effect of axial load (model 2) predicts a lower load than

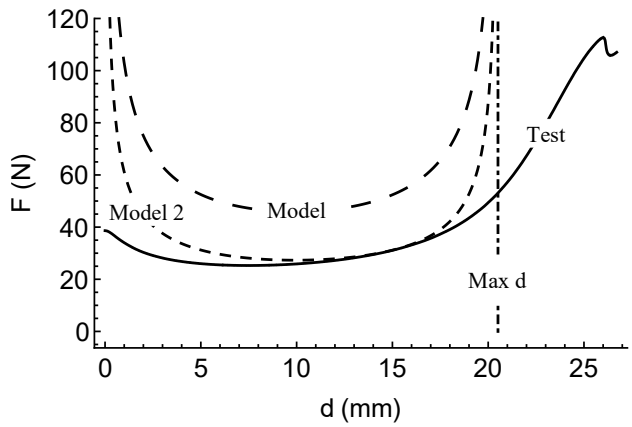

Figure 19: Comparison of experiment to model for a sector angle of $\Phi = 160°$ and $\rho = 0.8$, including consideration of axial load on inclined yield lines (model 2).

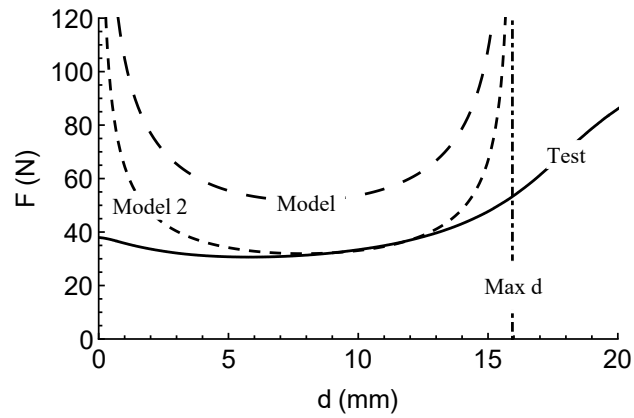

Figure 20: Comparison of experiment to model for a sector angle of $\Phi = 150°$ and $\rho = 0.8$, including consideration of axial load on inclined yield lines (model 2).

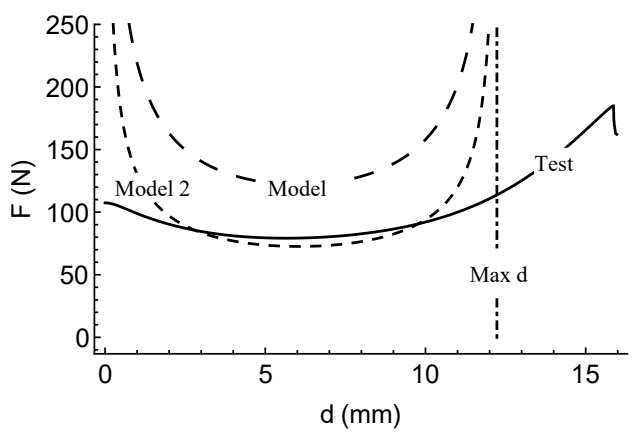

Figure 21: Comparison of experiment to model for a sector angle of $\Phi = 160°$ and $\rho = 0.6$, including consideration of axial load on inclined yield lines (model 2).

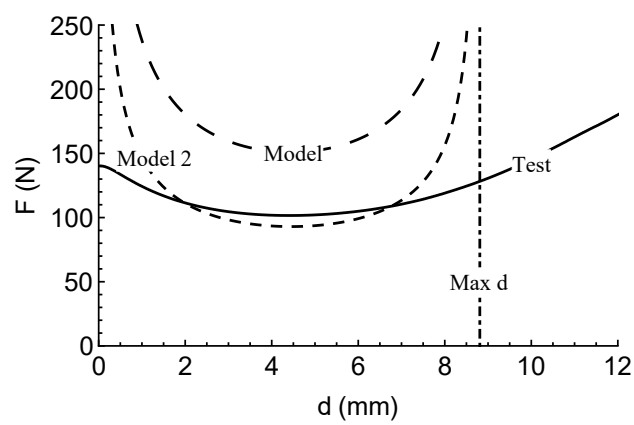

Figure 22: Comparison of experiment to model for a sector angle of $\Phi = 150°$ and $\rho = 0.6$, including consideration of axial load on inclined yield lines (model 2).

Eqn 14, but the extension limits remain the same since this is a kinematic constraint. In the cases considered

in this study the axial load reduces the predicted load to a similar range or lower than the measured load. Unfortunately, the deformation of the annuli adds additional complications to the calculation of the plastic moment capacity due to the presence of shear stresses as well as the changing orientation of the yield-lines during deformation, which are not included in the Hiriyur and Schafer model. More study is needed to fully understand the influence of the stress state on the plastic moment capacity of a yield line.